

Imaging extended single crystal lattice distortion fields with multi-peak Bragg ptychography

S. Kandel¹, S. Maddali^{2,*}, M. Allain³, X. Huang⁴, Y. S. G. Nashed^{5,**}, C. Jacobsen⁶, and S. O. Hruszkewycz^{2,†}

¹X-ray Science Division, Argonne National Laboratory, Lemont IL 60439, USA

²Materials Science Division, Argonne National Laboratory, Lemont IL 60439, USA

³Aix-Marseille Univ, CNRS, Centrale Marseille, Institut Fresnel, Marseille, France

⁴National Synchrotron Light Source II, Brookhaven National Laboratory, Upton, NY, 11973, USA

⁵Mathematics & Computer Science Division, Argonne National Laboratory, Lemont IL 60439, USA

⁶Department of Physics and Astronomy, Northwestern University, Evanston, IL 60208, USA

*Currently at KLA Corporation, CA (USA)

**Currently at Bristol Myers Squibb, NJ (USA)

†Corresponding author: shrus@anl.gov

Abstract

We describe a phase-retrieval-based imaging method to directly spatially resolve the vector lattice distortions in an extended crystalline sample by explicit coupling of independent Bragg ptychography data sets into the reconstruction process. Our method addresses this multi-peak Bragg ptychography (MPBP) inverse problem by explicit gradient descent optimization of an objective function based on modeling of the probe-lattice interaction, along with corrective steps to address spurious reconstruction artifacts. Robust convergence of the optimization process is ensured by computing exact gradients with the automatic differentiation capabilities of high-performance computing software packages. We demonstrate MPBP reconstruction with simulated ptychography data mimicking diffraction from a single crystal membrane containing heterogeneities that manifest as phase discontinuities in the diffracted wave. We show the superior ability of such an optimization-based approach in removing reconstruction artifacts compared to existing phase retrieval and lattice distortion reconstruction approaches.

1 Introduction

Bragg coherent diffraction imaging (BCDI) is a valuable tool to spatially resolve the lattice strain in crystalline materials at the scale of ~ 10 nm by using coherent x-rays as a probe [1, 2, 3]. Bragg ptychography, the scanning variant of BCDI, is used for extended crystalline samples larger than the beam size [4, 5, 6]. Both techniques have been applied to a variety of materials science problems, such as the performance of batteries [7, 8, 9], catalytic phenomena at metal interfaces [10, 11, 12, 13], and characterization of quantum sensors [14]. These conventional BCDI methods enable the spatial resolution of a single component of the three-component elastic lattice distortion field. This component corresponds to the Bragg diffraction vector of momentum transfer that comes about via a specific orientation of the single crystal lattice of the sample with respect to the beam (one of the crystal's Bragg conditions). Reorienting the crystal into other configurations with respect to the incident x-ray probe permits the independent components of the lattice distortion to be imaged. When three or more independent Bragg conditions can be satisfied and measured with BCDI, it is possible to unambiguously resolve the lattice displacement vector field within the sample.

Recent efforts to simultaneously reconstruct all components of internal lattice distortion fields with BCDI have shown promising results with simulations [15, 16] as well as experiments [17, 18]. The experimental works have employed different combinations of well-known fixed point iterative projection algorithms [19], typically in parallel reconstruction threads. The solutions of these parallel reconstructions are analyzed for desirable properties in order to seed the next generation of randomized solutions (*i.e.*, the ‘guided’ approach using genetic algorithms [20]). All the vector field reconstruction demonstrations referenced above explicitly minimize the discrepancy between the bulk distortion field and the computed phase from conventional phase retrieval. A recent alternate approach seeks to directly and simultaneously minimize the discrepancy in the measured and estimated coherent diffraction signals in

an all-encompassing gradient descent optimization scheme [21]. However, this specific approach pertains only to full coherent illumination of compact crystals, and the method is yet to be demonstrated on the relatively data-intensive Bragg ptychography problem with extended single-crystal samples.

We address the problem of multi-peak Bragg ptychography (MPBP) in this paper through simulations of independent ptychographic data sets and subsequent reconstruction of a two-dimensional projection of the underlying crystal lattice fields; this extends upon the preliminary work first recorded in [22]. The MPBP measurement approach follows that of Bragg projection ptychography [5, 23, 24] where, at a given angle that fulfills the Bragg condition, data is collected at multiple overlapping beam positions. In MPBP this process is repeated at different Bragg conditions. In terms of image reconstruction, MPBP employs a joint optimization scheme similar to [21] for all the measured ptychographic data sets corresponding to the independent Bragg conditions. Methods such as MPBP are poised to take advantage of the orders of magnitude increases in coherent flux at hard x-ray energies afforded by fourth-generation synchrotron light sources to image local displacement fields in crystals.

This paper is organized in the following manner: Section 2 introduces the MPBP forward model connecting the lattice distortion to the measured coherent diffraction signal for a single crystal. Section 3 lays out specifics of the numerical optimization problem, including the gradient descent scheme, the expected phase-wrap degeneracies in the solution and their resolution. Sections 4 and 5 describe the parameters of the numerical demonstrations in this paper, and the reconstruction results respectively. Section 6 closes with a discussion of the results and concluding remarks.

2 Forward model for multi-peak Bragg ptychography (MPBP)

We define a single-crystal sample in the laboratory frame (x_1, x_2, x_3) depicted in Figure 1, with the incident beam along the x_3 -direction. We adopt a sample geometry that mimics a crystalline free-standing membrane or a thin film affixed to a substrate with different lattice structure. Such systems are plentiful in the fields of functional materials [25] and micromechanical systems. Further, we note that in such systems where the membrane/film thickness is of order of ~ 100 nm, lateral heterogeneities in lattice characteristics over micrometer length scales are often of interest and through-thickness variations of strain are often minor by comparison.

The experiment that motivated the membrane model construction and the diffraction geometry considered in this work is described in [26]. In that work, a localized x-ray beam (11.8 keV energy) was oriented at near-normal incidence to a single crystal silicon membrane. By tuning the sample angle off of normal incidence by 15.9° , a Bragg reflection with hkl indices of 220 from the (110) lattice planes could be measured in a Laue geometry with a diffraction vector \mathbf{G}_{hkl} contained within the plane of the membrane. (Here, $\mathbf{G}_{hkl} = \mathbf{k}_i - \mathbf{k}_f^{hkl}$ with \mathbf{k}_i and \mathbf{k}_f^{hkl} being the wave vectors of the incident and exit x-ray beams, each with $|\mathbf{k}| = 1/\lambda$ where λ is the x-ray wavelength.) A Bragg ptychography image of a single component of the lattice displacement field in the two-dimensional plane of the membrane was reconstructed from a ptychography series of 220 Bragg peak intensity patterns. In the work we present here, we conceptualize an extension of the work of Takahashi *et al* by proposing multiple such measurements at different Bragg peaks with in-plane \mathbf{G}_{hkl} vectors (hkl reflections for which $l = 0$) and spatially resolving a lattice displacement field $\mathbf{u}(\mathbf{r})$ in terms of components U_1 and U_2 along the x_1 and x_2 in-plane spatial coordinates via global optimization.

As shown in Figure 1, for this work, a 3D membrane sample model with extended dimensions along x_1, x_2 and limited extent along x_3 was constructed. An inhomogeneous lattice displacement field $\mathbf{u}(x_1, x_2)$ was defined that was self-similar within the x_3 dimension of the membrane. A set of Bragg reflections with in-plane diffraction vectors were chosen with diverse in-plane orientation and different reciprocal space magnitudes. At each hkl Bragg reflection, the sample has a distinct scattering amplitude $\mathcal{X}_{hkl}(\mathbf{r})$ and can be described as a 3D complex-valued real-space object:

$$\phi_{hkl} = \mathcal{X}_{hkl}(\mathbf{r})e^{2\pi i \mathbf{u}(\mathbf{r})^T \cdot \mathbf{G}_{hkl}}. \quad (1)$$

where \cdot denotes a matrix multiplication. Since the Bragg peaks of interest all have $l = 0$, we ignore this Miller index in the subsequent text. For convenience, we represent the effective real-space object for each Bragg peak as a single column vector \mathcal{O}_{hk} obtained by concatenating the elements of ϕ_{hk} .

In the case of Bragg ptychography from a 3D crystal, the x-ray illumination function (or probe) is also 3D and varies with different Bragg peaks due to the different angles of incidence of the beam on the sample and the different orientations of the exit beam [27]. We denote the 3D probe that satisfies each Bragg diffraction condition as \mathcal{P}_{hk} based on a set of incident sample angles and exit beam orientations consistent with a cubic-structured crystal in a diffractometer equipped with a single rotation axis sample stage and a two-rotation-axis detector geometry typical of nanodiffraction beamlines. The 2D beam profile that was used to determine \mathcal{P}_{hk} was one reconstructed from experimental data of a test pattern illuminated with a nanofocused beam, as described in [28]. For convenience, we then construct a diagonal matrix $\text{diag}(\mathcal{P}_{hk})$ with the elements of \mathcal{P}_{hk} . Since the crystal is thin in the x_3 dimension and we seek to reconstruct a the 2D displacement field of the membrane, we do not require the information generated

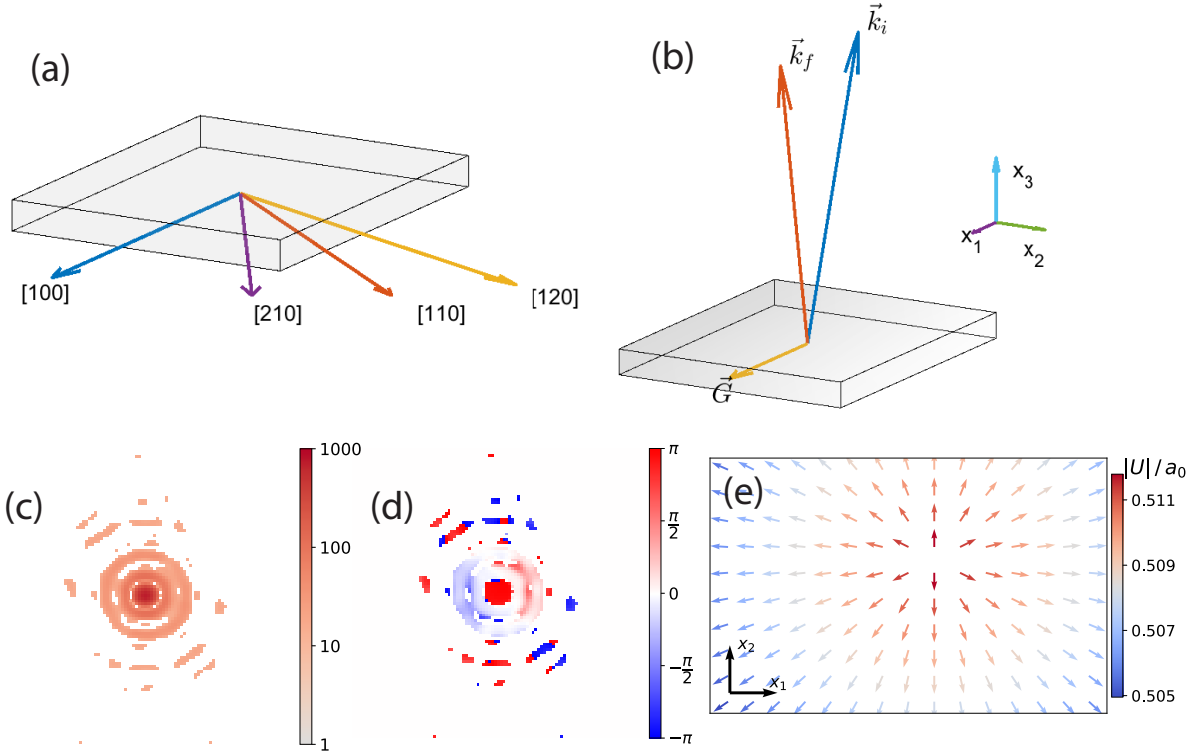


Figure 1: Illustration of (a) Bragg peaks of interest for the simulated thin crystal film, (b) incident (\mathbf{k}_i) and exit (\mathbf{k}_f) directions for the [100] Bragg peak (labelled \mathbf{G}), (c) magnitude of the probe beam along its propagation direction, (d) phase of the probe beam, and (e) the simulated radially decaying displacement profile (\mathbf{U}), where the direction of the arrows show the direction of the lattice displacement, and the color of the arrows show the magnitude of the displacement.

via an angular scan of the object about each Bragg angle. Therefore, for this experiment, the expected intensity at the far-field detector plane for each ptychographic scan position can be written as:

$$\mathbf{I}_{hk,j} = \|\mathcal{F} \cdot \mathcal{R}_{hk} \cdot \text{diag}(\mathcal{P}_{hk}) \cdot \mathcal{S}_{hk,j} \cdot \mathcal{O}_{hk}\|^2 + \mathbf{b}_{hk,j} \quad (2)$$

where j indexes the scan positions (with $1 \leq j \leq J$), $\mathcal{S}_{hk,j}$ is an operator that shifts the object laterally per scan position, $\mathbf{b}_{hk,j}$ is the background, and \mathcal{R}_{hk} is the operator that rotates and interpolates the 3D real-space illuminated object from the \mathbf{x}_1 - \mathbf{x}_2 - \mathbf{x}_3 coordinate reference frame to the detector reference frame for each Bragg reflection (which contains \mathbf{k}_f^{hk} as one of the orthonormal coordinate directions), then generates the 2D exit wave along the \mathbf{k}_f^{hk} direction. The construction of the forward model in (2) is modeled after the one presented in [28], where the operator \mathcal{R} is also described. These detector reference frames are typically different for each Bragg peak and, consequently, this interpolation is also different. Furthermore, this interpolation also needs to account for the fact that the sample-detector distance and the detector pixellation could be different for these different detector geometries—therefore the interpolated 2D object projection could have different voxel sizes as dictated by the Nyquist sampling condition—as well as other necessary coordinate transformations [29, 30]. Finally, by Fourier transforming (\mathcal{F}) the exit wave thus calculated, we generate multiple sets of diffraction patterns per Bragg reflection consistent with a sample being rastered in the beam in overlapping steps. We denote the measured intensities as $\mathbf{y}_{hk,j}$.

The forward model that we have developed has two key features. First, the *phase* in all the effective objects \mathcal{O}_{hk} (Equation (1)) is due to the *shared* (among all the Bragg peaks) displacement field, and this displacement field is what we aim to reconstruct. Second, the amplitudes (or magnitudes) of the objects for the different peaks differ only by a global scaling factor that varies with possible differences in the scattering strength of the sample at different Bragg peaks.

3 Solving the MPBP problem

To formulate the MPBP reconstruction algorithm, we first need to identify the variables we want to solve for, then define the error metric that we aim to minimize. For this work, we assume that the probe functions are known, that we obtain the intensity diffraction data at D different Bragg peaks, that the lateral dimensions of interest of the

membrane can be represented with $N_{x_1} \times N_{x_2}$ pixels, and that the membrane does not change along the x_3 direction. The variables we want to reconstruct are as follows:

- the $2N$ displacement variables represented by the matrix \mathbf{U} defined row-wise as $\mathbf{U}_n = (u_{x_1,n}, u_{x_2,n})$, where each row \mathbf{U}_n is the transpose of the displacement vector for the voxel n , and where $1 \leq n \leq N = N_{x_1} \times N_{x_2}$ indexes the voxels.
- the N per-pixel amplitude variables for the Bragg peak chosen as reference. We represent these variables as \mathcal{X} and note that $\mathcal{X} \geq 0$ elementwise. We note that any of the D Bragg peaks can serve equally as the reference peak.
- the $D - 1$ global scaling factors, represented by the vector $\boldsymbol{\alpha}$ (with $\boldsymbol{\alpha} > 0$ elementwise), that we use to scale the object magnitudes for the remaining Bragg peaks. These scaling factors simultaneously account for differences in scattering power of different Bragg peaks and differences in the measurement between Bragg peak ptychography scans (i.e. choice of exposure time).

We therefore have a total $3N + D - 1$ unknowns to solve for. We can write the objects (per Bragg peak) in terms of these variables as:

$$\mathbb{O}_{hk} = \begin{cases} \mathcal{X} e^{i\mathbf{U} \cdot \mathbf{G}_d} & \text{if } d = 1, \\ \alpha_{d-1} \mathcal{X} e^{2\pi i \mathbf{U} \cdot \mathbf{G}_d} & \text{otherwise,} \end{cases} \quad (3)$$

where \mathbf{G}_d denotes the scattering vector for the d th Bragg peak. We attempt to solve for these variables by minimizing the Gaussian error metric,

$$f(\mathbf{U}, \mathcal{X}, \boldsymbol{\alpha}) := \frac{1}{2} \sum_{hk,j} \left\| \mathbf{I}_{hk,j}^{1/2} - \mathbf{y}_{hk,j}^{1/2} \right\|^2. \quad (4)$$

The nonlinear minimization problem is then

$$\text{find } (\mathbf{U}_\star, \mathcal{X}_\star, \boldsymbol{\alpha}_\star) \in \underset{\mathbf{U} \in \mathbb{R}, \mathcal{X} \in \mathbb{R}_{\geq 0}, \boldsymbol{\alpha} \in \mathbb{R}_{> 0}}{\text{argmin}} f. \quad (5)$$

3.1 Ambiguities in the displacements: a challenging reconstruction problem

Previous works [31, 6, 28] have shown that the single-peak Bragg ptychographic phase retrieval problem can be solved using a gradient-descent-based update algorithm. However, the reconstruction of the crystal lattice displacement field, using either multiple such phase profiles (per Bragg peak) or directly from the diffraction datasets, is challenged by an implicit periodicity that leads to a preponderance of sub-optimal *local* minima in the landscape for the error metric (Equation (4)). This necessitates an adaptation so that gradient-descent-based iterative approaches can find the true solution. In this section, we first demonstrate how the lattice displacement reconstruction problem is affected by ambiguities, then propose a solution to address this challenge. While we focus this discussion on the MPBP setting, the arguments we develop apply to general Bragg coherent imaging of single-crystal lattice displacements.

We first consider the effective object for a single Bragg peak \mathbf{G}_1 , which can be written using several equivalent forms,

$$\mathbb{O}_1 = |\mathbb{O}_1| e^{2\pi i \mathbf{U}_\star \cdot \mathbf{G}_1} \quad (6a)$$

$$= |\mathbb{O}_1| e^{2\pi i (\mathbf{U}_\star \cdot \mathbf{G}_1 + \mathbf{m}_1)} \quad (\text{for any } \mathbf{m}_1 \in \mathbb{Z}^N) \quad (6b)$$

$$= |\mathbb{O}_1| e^{2\pi i \left(\mathbf{U}_\star + \frac{1}{\|\mathbf{G}_1\|^2} \mathbf{m}_1 \cdot \mathbf{G}_1^T \right) \cdot \mathbf{G}_1}, \quad (6c)$$

that are related to one another due to the inherent periodicity in the phases. In fact, the term $\mathbf{U}' = \left(\mathbf{U}_\star + \frac{1}{\|\mathbf{G}_1\|^2} \mathbf{m}_1 \cdot \mathbf{G}_1^T \right)$ in Equation (6c) represents a family of possible lattice displacements that are indistinguishable with respect to \mathbb{O}_1 . As a result, any choice of \mathbf{m}_1 gives rise to the same diffraction patterns as the true displacement \mathbf{U}_\star . As an example, we can look at the displacement field corresponding to

$$\mathbf{m}_1 = (1, 1, \dots, 1)^T \quad \text{or} \quad \mathbf{m}'_1 = (5, -5, 5, -5, \dots)^T. \quad (7)$$

The true displacement field \mathbf{U}_\star has $\mathbf{m}_1 = (0, 0, \dots, 0)$, yet the \mathbf{U} fields arising from \mathbf{m}_1 and \mathbf{m}'_1 both produce the same diffraction patterns. Moreover, \mathbf{m}'_1 is associated with a highly unphysical spatially discontinuous strain tensor. Consequently, we cannot distinguish the true displacement \mathbf{U}_\star from any \mathbf{U}' using data along just the Bragg peak \mathbf{G}_1 , even when $\mathbf{U}_\star \cdot \mathbf{G}_1 = 1$ so that the projection does not cause any loss of information. We illustrate this challenge in Figure 2: Figure 2a schematically depicts the family of displacements $\mathbf{u} \pm m\Delta \frac{\mathbf{G}_{110}}{\|\mathbf{G}_{110}\|^2}$ that would all lead to the same

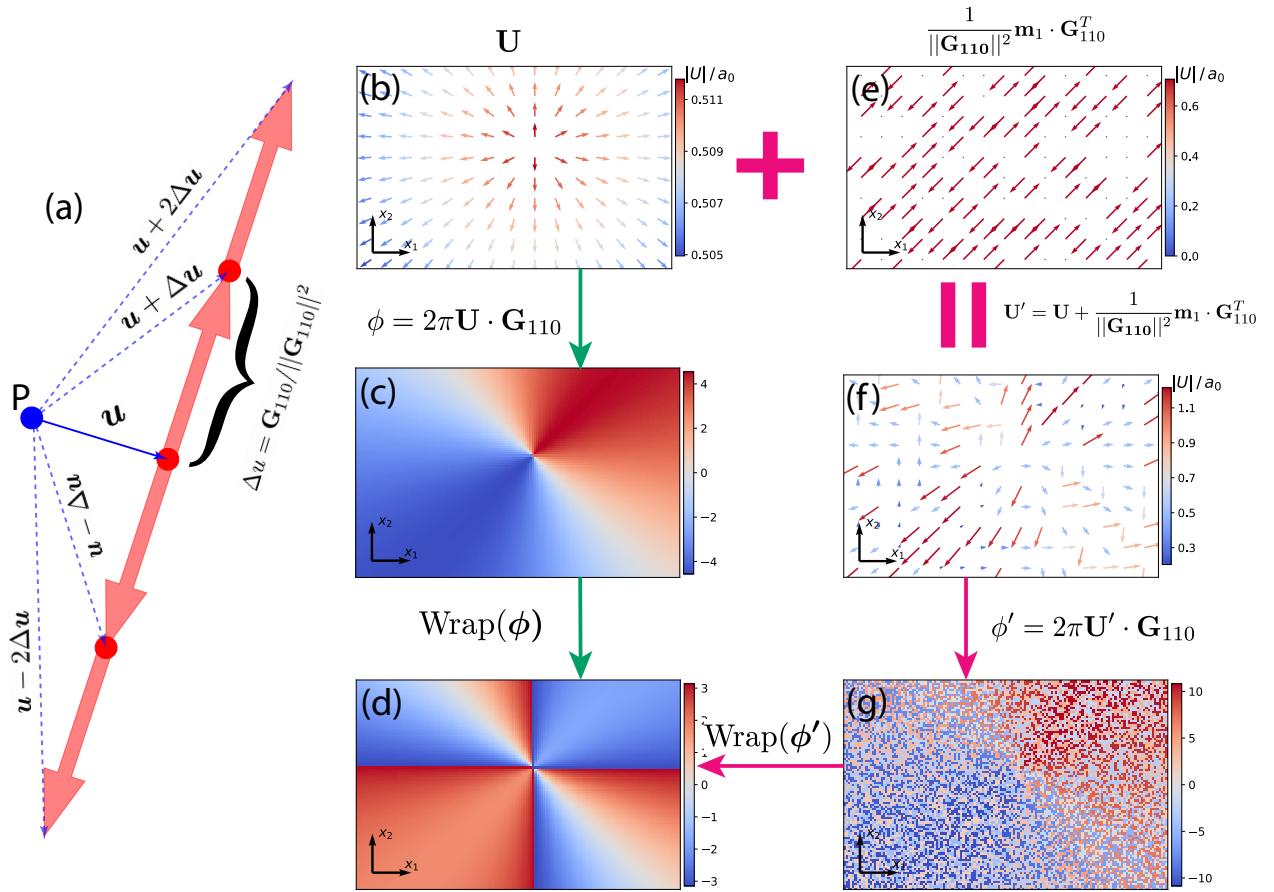


Figure 2: (a) A schematic representation of the ambiguity in the displacement vector at a given pixel. Considering the $[110]$ peak for example, at any location in the reconstruction field of view P , the displacements $\mathbf{u} + m\Delta\mathbf{u}$ (with m any integer) all give rise to the same phase value. (b) The true displacement profile (scaled by the lattice distance a_0) is associated with the unwrapped phase profile (c), which after wrapping gives the profile in (d). If we choose $m \in \{-1, 0, 1\}$ randomly for every point in the film, we get the field in (e). Adding the fields in (b) and (e), we get the unphysical displacement field (f) that is associated with the phase profile (g). After wrapping, the phase profile in (g) also gives the profile in (d). We therefore cannot distinguish between the displacement fields (b) and (f) based on the object phase for the \mathcal{G}_{110} peak alone.

\mathbf{G}_{110} phase for any pixel P , and Figure 2b-g show the effect of this per-pixel ambiguity for the 2D thin film lattice displacement profile of the membrane model under consideration.

Next, we examine the case in which we have diffraction data generated along two Bragg peaks \mathbf{G}_1 (for $(h_1, k_1, 0)$) and \mathbf{G}_2 (for $(h_2, k_2, 0)$). If $\mathbf{G}_1^T \cdot \mathbf{G}_2 = 0$, then $\mathbf{U}' \cdot \mathbf{G}_2 = \mathbf{U}_\star \cdot \mathbf{G}_2$, which means we again cannot isolate the summand \mathbf{U}_\star using just the diffraction data along these two Bragg peaks. When $\mathbf{G}_2^T \cdot \mathbf{G}_1 \neq 0$, the additional Bragg peak may reduce the set of ambiguities that are inherent to the single Bragg peak case. However, to our best knowledge, there is no formal proof that any combination of noise-free measurements about specific Bragg peaks provides an unambiguous solution for the problem. It is also likely that local minima exist for the minimization problem Equation (5). Since gradient-based methods can only guarantee convergence to local minima, applying these to the optimization problem in Equation (5) is prone to stagnation at these minima — we observe this in practice in the 4-peak MPBP simulation that we present subsequently.

Our analysis so far shows that the inherent ambiguities in the displacements lead to spurious global or local minima in the landscape for the error metric f (Equation (4)), and we propose the following heuristic solution to this challenge. We formulate our solution by noting that, in the MPBP forward model, we first project the pixelwise displacements \mathbf{U}_n through the operation $\phi(\mathbf{U}_n, \mathbf{G}_d) = 2\pi\mathbf{U}_n \cdot \mathbf{G}_d$ per Bragg peak \mathbf{G}_d . If we ignore any physics-based constraints, the elements of \mathbf{U} can attain any value in $(-\infty, \infty)$, and the range of $\phi(\mathbf{U}_n, \mathbf{G}_d)$ is also $(-\infty, \infty)$. In contrast, when we invert this model, we calculate these projection through the function $\phi_1^{\text{inv}}(\mathcal{C}_{1,n}) = \arctan(\Im[\mathcal{C}_{1,n}]/\Re[\mathcal{C}_{1,n}])$, the range of which is only $(-\pi, \pi)$. The gradient-based inversion program does not correct for this mismatch, leading to possibly incorrect \mathbf{U}_n values. A natural solution to this mismatch would then be to somehow change the range of $\phi_1^{\text{inv}}(\mathcal{C}_{1,n})$ to $(-\infty, \infty)$: we can achieve this through the phase unwrapping procedure [32]. Since the phase unwrapping procedure removes the 2π jumps in the phase map, they change the range of the phase map from $(-\pi, \pi)$ to $(-\infty, \infty)$. As

such, incorporating the phase unwrapping procedure within the MPBP optimization algorithm should be sufficient to correctly solve for the crystal displacements, and we demonstrate this with the subsequent numerical experiments.

3.2 CDI-based strain reconstruction methods in the literature

While we are not aware of any existing literature that specifically addresses the MPBP problem, there exist two primary classes of algorithms that reconstruct crystalline displacement (or strain) by combining the diffraction data obtained from multi-peak BCDI experiments: the classical *two-step* reconstruction methods (which are the methods of choice in the literature), and the newly developed *concurrent* reconstruction methods.

In the two-step reconstruction approach, one first reconstructs the full effective objects for the individual Bragg peaks, then uses the reconstructed phase profiles to obtain the displacement and strain profiles [33, 34, 35, 17]. This approach suffers from a number of technical challenges. First, it requires the initial solution of a total of $2ND$ magnitude and phase variables, which can be much higher than the $3N + D - 1$ variables that we actually require, and is therefore a harder inversion problem. If we have insufficient or noisy data along one of the Bragg peaks, then the corresponding object reconstruction can contain artifacts or fail altogether, and thereby significantly deteriorate our desired displacement and strain reconstructions. Second, while individual BCDI reconstructions are agnostic to translations of the real-space objects, we need to ensure that these individual real-space objects coincide to perform the displacement reconstructions, and aligning these can itself be a challenging problem [15].

In the concurrent reconstruction approach, we treat the diffraction data generated from multiple Bragg peaks as one dataset and use this dataset to simultaneously reconstruct the real-space objects and the displacement fields. While the existing works that use this approach [15, 16, 18] do not specifically solve for the variables we cataloged earlier in this section (*viz.*, the displacement, magnitude, and scaling variables), and solve for individual real-space objects instead, they share the information between these objects by also tracking the displacement profiles and the real-space support, thereby implicitly solving for the same $3N + D - 1$ variables instead of the full $2ND$ object variables.

The problem of reconstructing displacement fields that result in phase wraps has been handled in different ways in BCDI literature. In the two-step reconstruction approach, these phase maps have been first unwrapped before the displacement calculations, but, even so, the displacements so calculated are themselves often error-prone [20]. In a recent work, Hofmann *et al* [17] refine the basic two-step approach by using carefully designed phase offsets and working with phase gradients to directly reconstruct the strain tensors. On the one hand, this method is agnostic to any phase wrap issues. On the other hand, it solves for the much larger set of $2ND$ real-space object variables, introduces even more variables in the strain reconstruction step, and also requires a careful alignment of the real-space object reconstructions. Finally, Maddali *et al* [21] have recently developed a concurrent reconstruction approach that uses a median filter to minimize any distortions in the displacement field, but this approach may not resolve phase-wrap-associated artifacts at longer length scales and may also deteriorate the spatial resolution of the reconstruction. As such, a concurrent reconstruction approach that robustly addresses the model mismatch problem very desirable.

3.3 The MPBP reconstruction algorithm

In this section, we outline a MPBP reconstruction algorithm that, in contrast to the approaches described above (Section 3.2), directly solves for the desired displacement (\mathbf{U}), magnitude (\mathcal{X}), and scaling ($\boldsymbol{\alpha}$) variables, in a manner analogous to that developed in [21], but for the case considered here of ptychography data measured at multiple Bragg conditions, with specific adaptations aimed at the phase wrap problem.

To begin with, we note that magnitude and scaling variables should be constrained so that the $\mathcal{X} \geq 0$ and $\boldsymbol{\alpha} > 0$; ignoring these constraints in the optimization can lead to stagnation in the minimization. While it is certainly possible to apply these constraints (through projection steps, for example), we implement this constraint indirectly by defining the auxiliary variables $\tilde{\mathcal{X}} \in \mathbb{R}^N$ and $\tilde{\boldsymbol{\alpha}} \in \mathbb{R}^{D-1}$ that satisfy the relations

$$\mathcal{X} = e^{\tilde{\mathcal{X}}}, \quad \text{and} \quad \boldsymbol{\alpha} = e^{\tilde{\boldsymbol{\alpha}}}. \quad (8)$$

Solving for these auxiliary variables naturally enforces the constraints, and we can use a small threshold at the end of the optimization procedure to set $\mathcal{X} = 0$ in regions not illuminated by the probe.

We now define a $2 \times D$ matrix \mathbf{H} columnwise as $\mathbf{H}_{\bullet,d} = \begin{pmatrix} \mathbf{G}_d \cdot \mathbf{e}_1 \\ \mathbf{G}_d \cdot \mathbf{e}_2 \end{pmatrix}$, where \mathbf{e}_1 and \mathbf{e}_2 are the unit vectors along the \mathbf{x}_1 and \mathbf{x}_2 directions respectively. We can then simultaneously calculate the phases for all the real-space objects as

$$\boldsymbol{\Phi} = \mathbf{U} \cdot \mathbf{H}, \quad \text{and, conversely,} \quad \mathbf{U} = \boldsymbol{\Phi} \cdot \mathbf{H}^T \cdot (\mathbf{H} \cdot \mathbf{H}^T)^{-1}, \quad (9)$$

where $\boldsymbol{\Phi}$ is a $N \times D$ matrix whose columns contain the phase maps for the individual Bragg peaks, and where the second expression comes about because \mathbf{H} is a full-rank rectangular matrix. If we define a phase wrapping operation \mathcal{W} that simultaneously calculates the wrapped phase for all the real-space projections of the displacement field,

and we define the phase unwrapping operation \mathcal{W}^{-1} that simultaneously calculates the unwrapped phase for all the real-space objects, we can now define a projector:

$$\Pi_U(\mathbf{U}) = \mathcal{W}^{-1}\{\mathcal{W}\{\mathbf{U} \cdot \mathbf{H}\}\} \cdot \mathbf{H}^T \cdot (\mathbf{H} \cdot \mathbf{H}^T)^{-1}. \quad (10)$$

Under ideal circumstances, this projector takes the displacement field, which could contain the periodicity-induced discontinuities, calculates the associated phase maps, removes the discontinuities via the phase unwrapping procedure, then calculates the now artifact-free displacement fields, thereby addressing the minimization challenges we discussed in Section 3.1. We note that this is a heuristic operation that depends greatly on the properties of the chosen phase unwrapping algorithm, and could be error-prone in practical applications. However, we find that this projector, used within the reconstruction algorithm outlined below (Algorithm 1), works quite well in our numerical simulations.

Algorithm 1 Single iteration of the minibatch MPBP reconstruction algorithm

Require: Initial guesses \mathbf{U}^0 , $\tilde{\chi}^0$, $\tilde{\alpha}^0$.

Require: Minibatch size b .

- 1: Randomly shuffle the JD diffraction patterns irrespective of the J probe positions (per peak) and the D Bragg peaks.

$$\mathfrak{J} = \{1, 2, \dots, JD\} \xrightarrow{\text{shuffle}} \mathfrak{J}'$$

- 2: **for** $t = 1$ to JD/b **do**

- 3: With the diffraction patterns indexed as $j \in \mathfrak{J}'$, calculate the partial derivatives:

$$\partial_U f^t := \sum_{j=b(t-1)+1}^{bt} \partial_U f(\mathbf{U}_j^{t-1}), \quad (11a)$$

$$\partial_{\tilde{\chi}} f^t := \sum_{j=b(t-1)+1}^{bt} \partial_{\tilde{\chi}} f(\tilde{\chi}_j^{t-1}), \quad \text{and} \quad (11b)$$

$$\partial_{\tilde{\alpha}} f^t := \sum_{j=b(t-1)+1}^{bt} \partial_{\tilde{\alpha}} f(\tilde{\alpha}_j^{t-1}). \quad (11c)$$

- 4: Use these partial derivatives within the Adam algorithm [36] to calculate \mathbf{U}^t , $\tilde{\chi}^t$, and $\tilde{\alpha}^t$.
 - 5: Set $\mathbf{U}^t \rightarrow \Pi_U(\mathbf{U}^t)$.
 - 6: **end for**
-

We present the steps taken within a single iteration of our MPBP reconstruction approach in Algorithm 1 and note that this is a variation of the basic minibatch ptychography algorithm presented in [31][Algorithm 1]. However, the use of the \mathbf{U} , $\tilde{\chi}$, and $\tilde{\alpha}$ variables, instead of the $(\mathfrak{R}[\mathcal{O}], \mathfrak{I}[\mathcal{O}])$ variables in [31], for the gradient calculations requires extra coordinate transformations and other mathematical manipulation. Indeed, this adds to the already significant algebra that would be required to calculate the gradients just for the basic MPBP model. Therefore, by using the AD framework (which is implicit in Line 3 of Algorithm 1), we not only avoid such tedious and error-prone algebra, but also take advantage of the state-of-the-art parallelized implementations of the mathematical operations (including the complex interpolations) required for both the MPBP forward model and gradient calculations[31, 21, 37, 38].

4 Numerical experiment

To test our proposed reconstruction algorithm, we use a numerical experiment with the basic experimental parameters listed in Table 1, wherein we simulate a thin film with a cubic lattice structure, which has a radially decaying 2D lattice distortion field emanating from a point in the field of view. This would be consistent with the displacement field associated with a local stress concentration in a crystal membrane, for example. For convenience, we define an orthonormal “lab frame” with the axes $(\mathbf{x}_1, \mathbf{x}_2, \mathbf{x}_3)$ and with the voxel size $5.84 \times 5.84 \times 5.84$ cubic microns, in which the simulated membrane is centered at the origin, and is aligned with its surface along the \mathbf{x}_1 - \mathbf{x}_2 plane so that it has the dimensions of $137 \times 85 \times 17$ voxels. As discussed in [21], the voxelation in the lab frame needs to be fine enough to obtain faithful rendering of the object after interpolation and projection to the detector frames of each Bragg peak.

To create a simulated data set from this membrane, we perform numerical ptychography experiments at each of the [100], [110], [120], and [210] Bragg peaks for the cubic lattice. (In an experiment setting, the choice of available peaks is dictated by the symmetry of the underlying crystal.) The *magnitudes* of the real-space objects ($|\mathcal{O}_{hk}|$) are scaled from unity to 0.004, 0.0035, 0.0021 and 0.0010 for the [100], [110], [120], and [210] peaks respectively.

This set of scaling parameters was chosen arbitrarily and has the effect of creating differing levels of low count rate diffraction intensity patterns that yield appreciable shot noise when used to generate consistent Poisson counting statistics, as was done here. Using different scaling parameters also necessitates that the relative scaling factors be reconciled by the reconstruction algorithm via the variable α . We show the orientations of the chosen \mathbf{G}_{hk} vectors and the radial profile of simulated lattice displacement field in Figure 1, the individual components of the displacement in Figure 3, the phase maps along each of the Bragg peaks in Figure 4, and the magnitude maps in Figure 5.

Table 1: Experimental details

Parameter	Value
Wavelength	1.377 Å (9 keV)
Detector	150 × 150 pixels
Detector pixel size	55 μm
Sample detector distance	0.35 m
Film length (\mathbf{x}_1)	0.8 μm
Film width (\mathbf{x}_2)	0.5 μm
Film thickness (\mathbf{x}_3)	0.1 μm
Lattice distance (cubic)	3.905 Å
Numerical window ($\mathbf{x}_1, \mathbf{x}_2, \mathbf{x}_3$)	200 × 200 × 100 voxels

In our ptychography simulations, we use a 2D probe profile experimentally measured from a Fresnel zone plate x-ray focusing optic at the HXN beamline at NSLS-II [39], of size 100 × 100 pixels at focus (with each pixel of size 1 nm). We threshold to zero any pixels in the probe below an intensity cutoff of 2% of the maximum intensity to reduce aliasing in the simulated diffraction patterns. Using the HXN diffractometer geometry, we calculated the set of sample incident angles and detector position exit angles that satisfy the Laue condition for each of the Bragg peaks of interest. For each peak, we interpolate the probe to produce the 3D illumination volume at the appropriate incident angle, with the beam profile set to be constant along the propagation direction through the numerical window. We then scan the thin film using a 9 × 9 grid, with a step size of 6 pixels, along the \mathbf{x}_1 - \mathbf{x}_2 plane. At every beam position, a diffraction pattern is generated by applying the forward model in (2), the scaling values discussed above were applied, and Poisson noise was added. The mean count rates of the diffraction patterns at each Bragg peak were ~ 83, 65, 52, and 12 photons per detector pixel respectively.

During the reconstruction, we solved for an \mathbf{x}_1 - \mathbf{x}_2 area of 147 × 95 pixels, stacked appropriately to produce the 3D membrane structure, initialized as an array of zeros, and placed centrally in the numerical window. The film support along the \mathbf{x}_1 and \mathbf{x}_2 directions are set to be 5 pixels larger than the actual film dimensions to allow for limited resolution effects due to the low photon count [40]. We performed reconstructions of the simulated data set using the following reconstruction approaches in order to enable a direct comparison of results:

- **TS**: the two-step approach (Section 3.2), where we first solve for the individual real-space objects (for each Bragg peak), unwrap the phases calculated for these objects, then calculate the displacements from the unwrapped phases. We use the AD-based approach described in Algorithm 1, but with the $4N$ phase variables (denoted as ϕ_{hk}) instead of the $2N$ displacement variables, and with the initial Adam update step sizes set to 0.01, 0.1 and 0.1 for the ϕ_{hk} , $\tilde{\mathcal{X}}$, and $\tilde{\alpha}$ variables respectively. We thereby solve for each of the real-space objects while utilizing the shared magnitude information between the objects.
- **C-W**: the concurrent-wrapped approach that uses the basic algorithm in Algorithm 1 but without any phase unwrapping, *i.e.*, without the projection step (in Line 5), and with the Adam update sizes set to 0.01, 0.1 and 0.1 for the \mathbf{U} , $\tilde{\mathcal{X}}$, and $\tilde{\alpha}$ variables respectively. In this test, no additional strategies such as local smoothing filters aimed to mitigate phase wrap discontinuities were implemented to represent baseline performance of this algorithm.
- **C-UW**: the concurrent-unwrapped approach outlined in Algorithm 1. For the phase unwrapping step, we use the algorithm [32] implemented within the “scikit-image” platform [41]. The Adam update sizes are set to 0.01, 0.1 and 0.1 for the \mathbf{U} , $\tilde{\mathcal{X}}$, and $\tilde{\alpha}$ variables respectively.

All the reconstructions used a minibatch size of 50 diffraction patterns, for a total of 1000 iterations of reconstruction. The update step sizes and the minibatch sizes were obtained through the trial and error approach outlined in [31]. The calculations were performed using the Tensorflow AD platform [42].

5 Results

In Figures 3–5 we present the reconstructions obtained for the lattice displacement, the phase maps, and the magnitude maps respectively. First, we examine the TS case, where Figures 4 and 5 show that the individual real-space

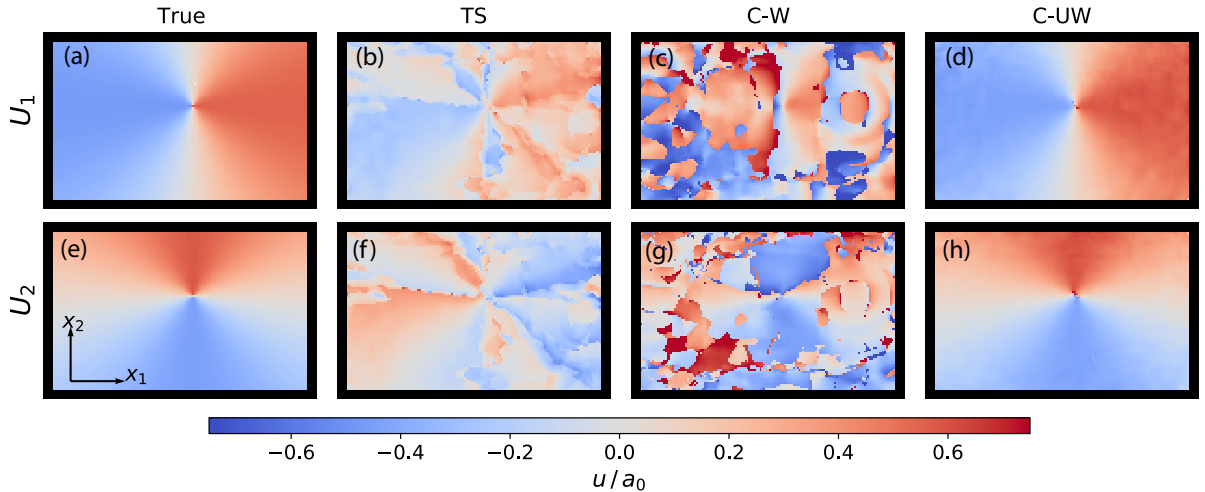


Figure 3: Reconstructed displacement components. (a,e) Simulated (true) values. The reconstructions obtained through the (b,f) two-step (TS) reconstruction method and the (c,g) concurrent method without the phase unwrapping step (C-W) show significant artifacts. The (d,h) concurrent-unwrapped (C-UW) reconstructions show close agreement with the true values.

object reconstructions are highly inaccurate, with artifacts for both phase and magnitude maps that are most pronounced in regions with phase discontinuities. The locations of these phase discontinuities are different for the real-space objects from each of the Bragg conditions. In these regions, the magnitude maps show "gaps" (regions of low magnitude)—a reconstruction artifact that has been observed previously in the literature [16, 43, 44]. As a consequence, the displacement calculated from the real-space phase maps are also discontinuous and inaccurate, as shown in Figure 3(b,f).

Next, we can see that the C-W reconstructions, where we directly reconstructed the displacement and magnitude maps without accounting for phase wrapping, show significant discontinuities in the displacement reconstructions (Figure 3(c,g)). Similarly, the phase maps (Figure 4(c,g,k,o)) and the reconstructed amplitudes projected to the \mathbf{G}_{hk} vectors (Figure 5(c,g,k,o)) both show prominent artifacts. The similarity of the artifacts in the magnitudes of the C-W reconstruction arise because in this approach the magnitude is scaled and shared among all Bragg peaks.

Finally, we can see that C-UW reconstructions algorithm accurately reproduces the simulated displacement and magnitude maps. In particular, while the magnitude maps (Figure 5) still contain a gap in the location of the stress concentration, they do not have either the strong phase artifacts (seen in the TS reconstructions) or the circular artifact (seen in the C-W reconstructions). The reconstructed displacement maps, and consequently the phase maps, are artifact-free.

6 Discussion and conclusion

In summary, we propose a multi-peak Bragg ptychography reconstruction framework to combine diffraction ptychographic datasets generated at multiple Bragg reflections to image the full lattice displacement and strain profiles. The results in Figures 3–5 demonstrate that our proposed approach can reconstruct both the displacement and the real-space magnitude profiles measured in the MPBP experiment. Compared to the TS procedure, this algorithm: i) significantly reduces the number of variables of interest, which makes for a more robust reconstruction, and ii) efficiently utilizes diffraction datasets that could be insufficient for individual real-space object reconstructions. By incorporating the phase unwrapping step, this algorithm also addresses the periodicity-driven model mismatch in the MPBP problem.

To apply the proposed algorithm to general experiment datasets, we need to be mindful about a few different aspects of the algorithm. First, we note that phase unwrapping is itself a difficult problem, particularly for objects with steep phase changes. Moreover, while our 2D phase unwrapping problem can be solved efficiently [32], its 3D extension can be significantly more time consuming [45, 46] and difficult to solve. In this context, it could be preferable to replace the phase unwrapping procedure altogether with a direct physics-based solution to the periodicity-driven model mismatch problem. Second, the reconstruction could contain unexpected artifacts if the datasets along the different peaks have significantly different photon counts (as we observe for the C-W case in the current work), in which case reweighing the diffraction datasets could produce more optimal results. Third, registry of the fields of view scanned at the different Bragg angles is imperative for this approach and has been realized in Bragg scanning nanodiffraction experiments by use of fluorescing fiduciary marks intentionally deposited on the

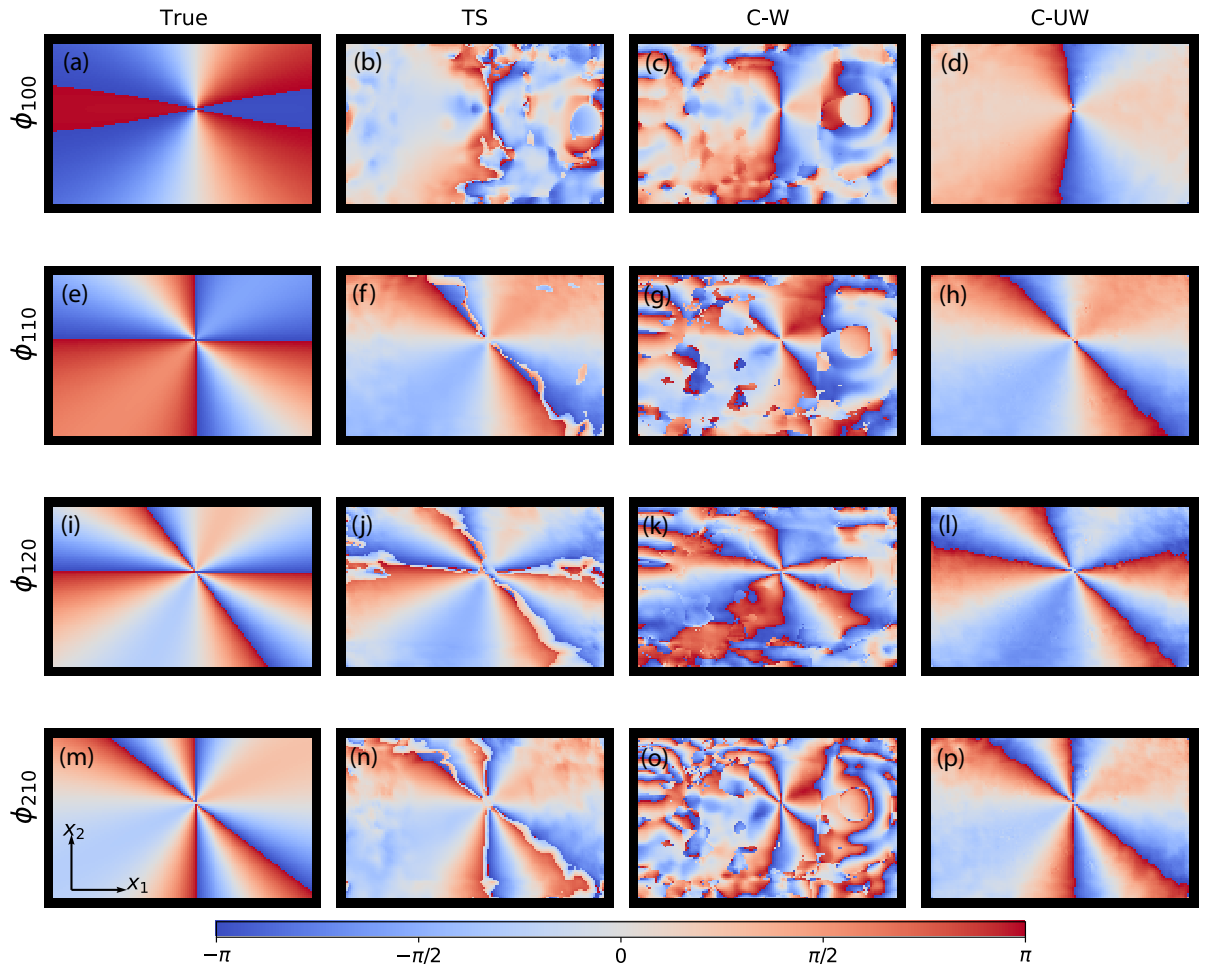


Figure 4: Reconstructed phase maps for each Bragg peak. (a,e,i,m) Simulated (true) values. The (b,f,j,n) TS phase maps and the (c,g,k,o) C-W phase maps show significant artifacts primarily at locations coinciding with discontinuous phase jumps (for both the TS and C-W cases), and other unrelated locations (for the C-W case). The C-UW phase maps agree closely with the true values.

sample surface. Finally, the reconstruction procedure is sensitive to the choice of the optimization hyperparameters, which therefore require careful tuning. We hope to address this in the future by designing more robust second order minibatch optimization procedures [37].

Since the proposed algorithm is simple in concept, it can be either incorporated within existing concurrent multi-peak BCDI workflows, or extended (via the AD framework) for applications in general BCDI or Bragg ptychography experimental models. We can also envision straightforward applications of the proposed method to simpler experimental models, such as the recently demonstrated “simultaneous” multi-Bragg peak CDI experiments [47]. In general, we expect that our algorithm marks a concrete step in connecting the ever-improving coherence of synchrotron sources to characterization of functional materials under real-world working conditions.

7 Acknowledgements

This work (concept development, forward model development, algorithm design) was supported by the U.S. Department of Energy (DOE), Office of Science, Basic Energy Sciences, Materials Science and Engineering Division. Algorithm testing was supported by the Laboratory Directed Research and Development (LDRD) funding from Argonne National Laboratory, provided by the Director, Office of Science, of the U.S. Department of Energy under Contract No. DE-AC02-06CH11357. We gratefully acknowledge the computing resources provided on Swing, a high-performance computing cluster operated by the Laboratory Computing Resource Center at Argonne National Laboratory. This research uses the resources of the Advanced Photon Source, a U.S. DOE Office of Science User Facility operated for the DOE Office of Science by Argonne National Laboratory under contract No. DE-AC02-06CH11357. This research used the 3-ID Hard X-ray Nanoprobe (HXN) beamline of the National Synchrotron Light Source II, a U.S. Department of Energy (DOE) Office of Science User Facility operated for the DOE Office of Science

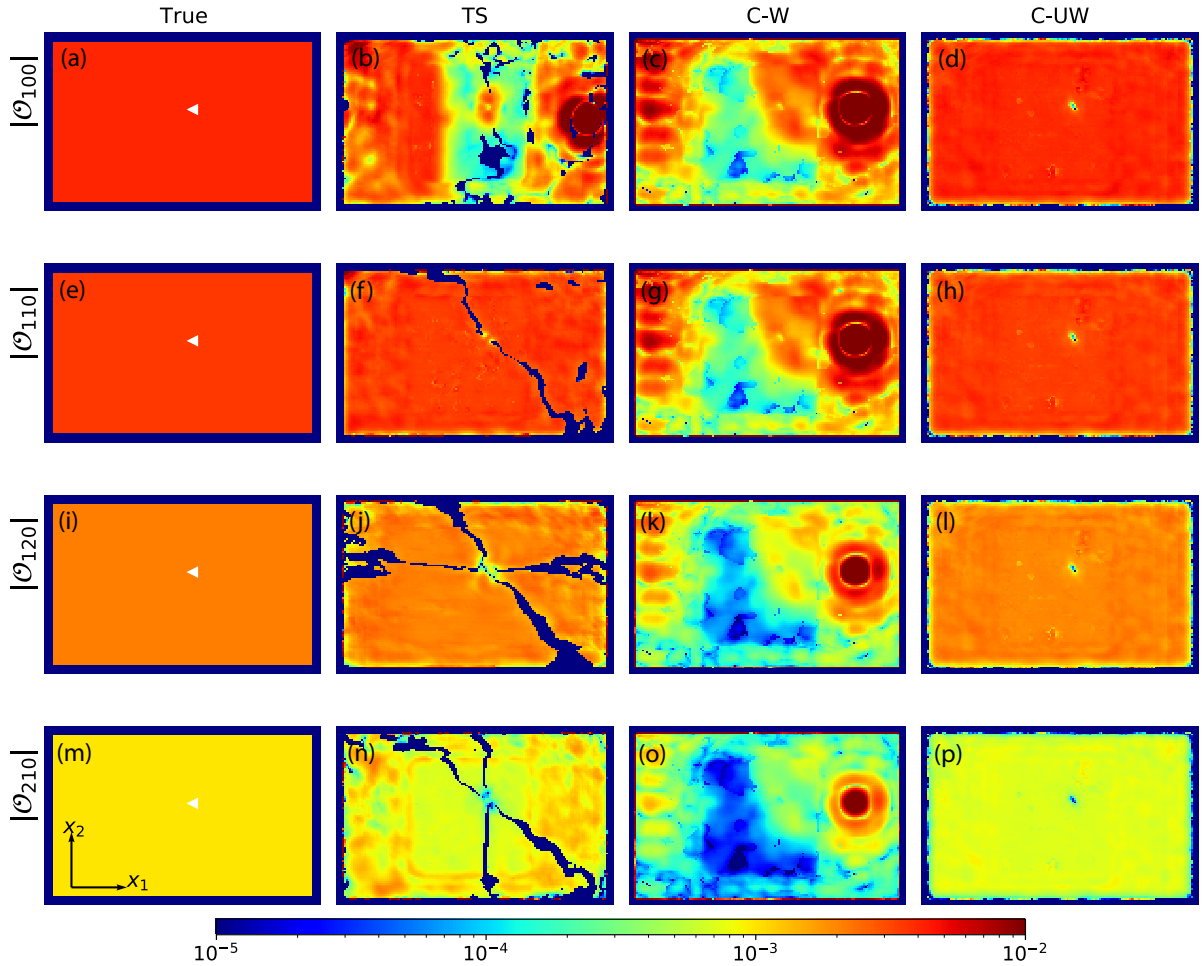


Figure 5: Reconstructed magnitude maps for each Bragg peak. (a,e,i,m) Simulated (true) values, where the white triangle indicates the location of the point distortion in the lattice displacements. The (b,f,j,n) TS magnitude maps, which are reconstructed individually for each Bragg peak, are inaccurate primarily at locations coinciding with discontinuous phase jumps. Among the (c,g,k,o) C-W and (d,h,l,p) C-UW methods, which both reconstruct a reduced number of magnitude variables, the C-W results contain major artifacts while the C-UW results maps agree closely with the true values.

by Brookhaven National Laboratory under Contract No. DE-SC0012704.

References

- [1] I. Robinson and R. Harder. “Coherent X-ray diffraction imaging of strain at the nanoscale”. In: *Nature Materials* 8 (2009), pp. 291–298.
- [2] I.K. Robinson and J.W. Miao. “Three-dimensional coherent x-ray diffraction microscopy”. In: *MRS Bulletin* 29.3 (2004), pp. 177–181.
- [3] I.K. Robinson and I.A. Vartanyants. “Use of coherent X-ray diffraction to map strain fields in nanocrystals”. In: *Applied Surface Science* 182.3-4 (2001), pp. 186–191.
- [4] Pierre Godard et al. “Three-dimensional high-resolution quantitative microscopy of extended crystals”. In: *Nature Communications* 2 (2011), p. 568.
- [5] S O Hruszkewycz et al. “Quantitative nanoscale imaging of lattice distortions in epitaxial semiconductor heterostructures using nanofocused X-ray Bragg projection ptychography”. In: *Nano Letters* 12.10 (Oct. 2012), pp. 5148–5154.
- [6] S. O. Hruszkewycz et al. “High-resolution three-dimensional structural microscopy by single-angle Bragg ptychography”. In: *Nature Materials* 16.2 (Feb. 2017), pp. 244–251. ISSN: 1476-1122. DOI: 10.1038/nmat4798. eprint: 1506.01262.

- [7] Andrew Ulvestad et al. “Single particle nanomechanics in operando batteries via lensless strain mapping”. In: *Nano Letters* 14.9 (2014), pp. 5123–5127.
- [8] Andrew Ulvestad et al. “Topological defect dynamics in operando battery nanoparticles”. In: *Science* 348.6241 (2015), pp. 1344–1347.
- [9] Andrej Singer et al. “Nucleation of dislocations and their dynamics in layered oxide cathode materials during battery charging”. In: *Nature Energy* 3.8 (2018), pp. 641–647.
- [10] Vladimir Komanicky et al. “Electrocatalytic activity of surface oxides on platinum nanofacets and surfaces”. In: *Electrochimica Acta* 109 (2013), pp. 440–446.
- [11] Wonsuk Cha et al. “Dealloying in individual nanoparticles and thin film grains: a Bragg coherent diffractive imaging study”. In: *Advanced Functional Materials* 27.25 (2017), p. 1700331.
- [12] Tomoya Kawaguchi et al. “Gas-induced segregation in pt-rh alloy nanoparticles observed by in situ bragg coherent diffraction imaging”. In: *Physical review letters* 123.24 (2019), p. 246001.
- [13] Tomoya Kawaguchi et al. “Study of the Internal Compositions of Binary Alloy Pd-Rh Nanoparticles by Using Bragg Coherent Diffraction Imaging”. In: *Journal of the Korean Physical Society* 75 (2019), pp. 528–533.
- [14] SO Hruszkewycz et al. “Strain annealing of SiC nanoparticles revealed through Bragg coherent diffraction imaging for quantum technologies”. In: *Physical Review Materials* 2.8 (2018), p. 086001.
- [15] Marcus C Newton. “Concurrent phase retrieval for imaging strain in nanocrystals”. In: *Physical Review B* 102.1 (2020), p. 014104.
- [16] Yuan Gao et al. “Bragg coherent diffraction imaging by simultaneous reconstruction of multiple diffraction peaks”. In: *Physical Review B* 103.1 (2021), p. 014102.
- [17] Felix Hofmann et al. “Nanoscale imaging of the full strain tensor of specific dislocations extracted from a bulk sample”. In: *Physical Review Materials* 4.1 (2020), p. 013801.
- [18] Matthew J Wilkin et al. “Experimental demonstration of coupled multi-peak bragg coherent diffraction imaging with genetic algorithms”. In: *Physical Review B* 103.21 (2021), p. 214103.
- [19] Stefano Marchesini. “A unified evaluation of iterative projection algorithms for phase retrieval”. In: *Review of Scientific Instruments* 78.1 (Jan. 2007), p. 011301.
- [20] A Ulvestad et al. “Identifying defects with guided algorithms in bragg coherent diffractive imaging”. In: *Scientific Reports* 7.1 (2017), pp. 1–9.
- [21] Siddharth Maddali et al. “Concurrent multi-peak Bragg coherent x-ray diffraction imaging of 3D nanocrystal lattice displacement via global optimization”. In: *npj Computational Materials* 9.1 (2023), p. 77.
- [22] Saugat Kandel. “Using automatic differentiation for coherent diffractive imaging applications”. PhD thesis. Northwestern University, 2021.
- [23] S O Hruszkewycz et al. “Imaging Local Polarization in Ferroelectric Thin Films by Coherent X-Ray Bragg Projection Ptychography”. In: *Physical Review Letters* 110.17 (Apr. 2013), p. 177601.
- [24] SO Hruszkewycz et al. “Structural sensitivity of x-ray Bragg projection ptychography to domain patterns in epitaxial thin films”. In: *Physical Review A* 94.4 (2016), p. 043803.
- [25] Xinghan Guo et al. “Tunable and transferable diamond membranes for integrated quantum technologies”. In: *Nano Letters* 21.24 (2021), pp. 10392–10399.
- [26] Yukio Takahashi et al. “Bragg x-ray ptychography of a silicon crystal: Visualization of the dislocation strain field and the production of a vortex beam”. In: *Physical Review B* 87.12 (2013), p. 121201.
- [27] Stephan O Hruszkewycz et al. “Efficient modeling of Bragg coherent x-ray nanobeam diffraction”. In: *Optics Letters* 40.14 (2015), pp. 3241–3244.
- [28] Megan O Hill et al. “Measuring three-dimensional strain and structural defects in a single InGaAs nanowire using coherent x-ray multiangle Bragg projection ptychography”. In: *Nano Letters* 18.2 (2018), pp. 811–819.
- [29] Peng Li et al. “General approaches for shear-correcting coordinate transformations in Bragg coherent diffraction imaging. Part II”. In: *Journal of Applied Crystallography* 53.2 (2020).
- [30] Siddharth Maddali et al. “General approaches for shear-correcting coordinate transformations in Bragg coherent diffraction imaging. Part I”. In: *Journal of Applied Crystallography* 53.2 (2020).
- [31] Saugat Kandel et al. “Using automatic differentiation as a general framework for ptychographic reconstruction”. In: *Optics Express* 27.13 (2019), pp. 18653–18672.
- [32] Miguel Arevallilo Herráez et al. “Fast two-dimensional phase-unwrapping algorithm based on sorting by reliability following a noncontinuous path”. In: *Applied Optics* 41.35 (2002), pp. 7437–7444.

- [33] Ian Robinson and Ross Harder. “Coherent X-ray diffraction imaging of strain at the nanoscale”. In: *Nature Materials* 8.4 (2009), pp. 291–298.
- [34] Marcus C Newton et al. “Three-dimensional imaging of strain in a single ZnO nanorod”. In: *Nature Materials* 9.2 (2010), pp. 120–124.
- [35] Julian Stangl et al. *Nanobeam X-ray Scattering: Probing Matter at the Nanoscale*. John Wiley & Sons, 2013.
- [36] Diederik P. Kingma and Jimmy Ba. “Adam: A method for stochastic optimization”. In: *CoRR* abs/1412.6980 (2014). arXiv: 1412.6980.
- [37] Saugat Kandel et al. “Efficient ptychographic phase retrieval via a matrix-free Levenberg-Marquardt algorithm”. In: *Optics Express* 29.15 (2021), pp. 23019–23055.
- [38] Ming Du et al. “Adorym: a multi-platform generic X-ray image reconstruction framework based on automatic differentiation”. In: *Optics Express* 29.7 (2021), pp. 10000–10035.
- [39] Yong Chu et al. *Hard x-ray nanoprobe facility at the National Synchrotron Light Source II*. Tech. rep. Brookhaven National Lab.(BNL), Upton, NY (United States), 2015.
- [40] V Chamard et al. “Strain in a silicon-on-insulator nanostructure revealed by 3D x-ray Bragg ptychography”. In: *Scientific Reports* 5 (2015), p. 9827.
- [41] Stéfan van der Walt et al. “scikit-image: image processing in Python”. In: *PeerJ* 2 (June 2014), e453. ISSN: 2167-8359. DOI: 10.7717/peerj.453.
- [42] Martín Abadi et al. “TensorFlow: large-scale machine learning on heterogeneous distributed systems”. In: *CoRR* abs/1603.04467 (2016). arXiv: 1603.04467.
- [43] Xiaojing Huang et al. “Propagation uniqueness in three-dimensional coherent diffractive imaging”. In: *Physical Review B* 83.22 (2011), p. 224109.
- [44] Marcus C Newton et al. “Phase retrieval of diffraction from highly strained crystals”. In: *Physical Review B* 82.16 (2010), p. 165436.
- [45] Hussein Abdul-Rahman et al. “Fast three-dimensional phase-unwrapping algorithm based on sorting by reliability following a non-continuous path”. In: *Optical Measurement Systems for Industrial Inspection IV*. Vol. 5856. International Society for Optics and Photonics. 2005, pp. 32–40.
- [46] R Cusack and N Papadakis. “New robust 3-D phase unwrapping algorithms: application to magnetic field mapping and undistorting echoplanar images”. In: *Neuroimage* 16.3 (2002), pp. 754–764.
- [47] Florian Lauraux et al. “Simultaneous multi-Bragg peak coherent x-ray diffraction imaging”. In: *Crystals* 11.3 (2021). ISSN: 20734352.